# Aggregation-Induced Structure Transition of Protein-Stabilized Zinc/Copper Nanoclusters for Amplified Chemiluminescence

Hui Chen,[†,‡] Ling Lin,[§] Haifang Li,[‡] Jianzhang Li,[†] and Jin-Ming Lin*,[‡]

[†]MOE Key Laboratory of Wooden Material Science and Application, Beijing Forestry University, Beijing, 100083, China, [‡]Department of Chemistry, Beijing Key Laboratory of Microanalytical Methods and Instrumentation, The Key Laboratory of Bioorganic Phosphorus Chemistry & Chemical Biology, Tsinghua University, Beijing, 100084, China, and [§]Faculty of Engineering, The University of Tokyo, Tokyo 113-8654, Japan

ABSTRACT A stable, water-soluble fluorescent Zn/Cu nanocluster (NC) capped with a model protein, bovine serum albumin (BSA), was synthesized and applied to the reaction of hydrogen peroxide and sodium hydrogen carbonate. A significantly amplified chemiluminescence (CL) from the accelerated decomposition of peroxymonocarbonate (HCO_4^-) by the nanosluster was observed. The CL reaction led to a

structure change of BSA and aggregation of Zn/Cu NCs. In the presence of H_2O_2, Zn/Cu—S bonding between BSA scaffolds and the encapsulated Zn/Cu@BSA NC was oxidized to form a disulfide product. Zn/Cu@BSA NCs were prone to aggregate to form larger nanoparticles without the protection of scaffolds. It is revealed that the strong CL emission was initiated from the catalysis of Zn/Cu@BSA NC and the surface plasmon coupling of the formed Zn/Cu nanoparticles in a single chemical reaction. This amplified CL was successfully exploited for selective sensing of hydrogen peroxide in environmental samples.
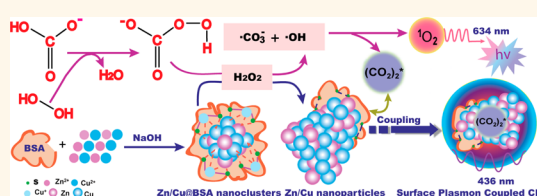
KEYWORDS: nanoclusters · nanoparticles · surface plasmon resonance · fluorescence · chemiluminescence

Metal nanoclusters (NCs) are nanometer core sized clusters composed of several to tens of atoms, most often luminescent in the visible region, and possess fascinating photophysical and chemical properties. Their sizes are comparable to the de Broglie wavelength of the electron at the Fermi energy of the metal. Electronic confinement in metal nanoclusters results in molecule-like properties such as discrete electronic states and size-tunable fluorescence.[1] The nanoclusters provide a missing link between atomic and nanoparticle (NP) behavior in metals, and the fluorescence of metal nanoclusters with ultrasmall size has attracted much interest in the field of chemistry, materials, and biology.[2−4]

Moreover, the clusters are extremely reactive in nature and tend to agglomerate without protection groups.[5] Therefore, the sophisticated design of protection groups or scaffolds is required to obtain water-soluble luminescent clusters. Within the past few years, luminescent gold and silver nanoclusters have been extensively studied for biolabeling and bioimaging applications due to their ultrafine size and nontoxicity.[6−10] A large variety of emitters in diverse scaffolds such as peptides,[11] DNA,[12−14] thiols,[15,16] protein,[17−19] and cells[20] have been reported. The use of a biomolecule as a template or scaffold for synthesis of nanoclusters possesses many advantages in biologically motivated applications.[21,22] Wen reported that dual functional fluorescent Au NCs formed *in situ* through horseradish peroxidase as a scaffold can be applied to hydrogen peroxide detection combining the catalysis function of the enzyme shell and the fluorescence of the core.[23] However, to date, only a few studies have given direct insight into zinc and copper nanoclusters because of the difficulty in preparing stable and highly luminescent Zn and Cu particles.[24−28] An effective approach to rationally designing a tiny zinc−copper bimetal nanocluster with functional ligands to give it broad applications remains to be explored.
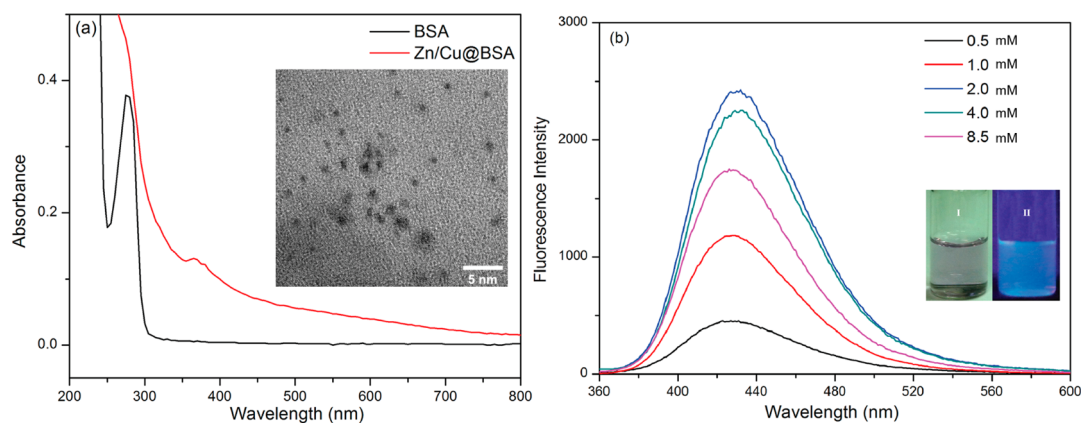
Figure 1. Characterization of Zn/Cu@BSA NCs. (a) UV−vis absorption spectra of Zn/Cu@BSA NCs (red line) and BSA solution (black line). Inset: TEM image of Zn/Cu@BSA NCs. (b) fluorescence spectra (λ_{ex} = 350 nm) for Zn/Cu@BSA NCs prepared from different initial metal ion concentrations ([Cu^{2+}]:[Zn^{2+}] = 1:1, mM), i.e., (1) 0.5, (2) 1.0, (3) 2.0, (4) 4.0, and (5) 8.5. Inset: Photographs of Zn/Cu@BSA NCs under visible light (I) and 365 nm UV light (II).

Recently, great attention has been paid to metal nanoclusters due to their stable structures and high luminescence. Compared to metal nanoparticles, the cluster-based active sites can serve as catalysts, and new properties emerging from the structure change in chemical reactions, such as the presence of surface plasmons, have been less discussed.[29−31] The catalysis of metal nanomaterials and the coupling effect of surface plasmons are able to accelerate the kinetics of chemiluminescence (CL) and improve the CL quantum yield.[32,33] In that sense, metal nanoclusters are able to be considered as potential CL emitters or as a novel alternative to catalyze redox CL reactions, enhancing the CL emission under proper conditions. This will not only open a new field for the development of novel CL-emitting species but also expand the conventional optical utilization of metal nanoclusters.

The ultraweak CL from the decomposition of peroxymonocarbonate (HCO_4^-), which is formed in equilibrium with hydrogen peroxide and bicarbonate, has been observed by our group.[34,35] It is significant to study the formation of HCO_4^- for the damage due to biothiol peroxidation considering the ubiquity of CO_2/HCO_3^- buffers in biology and the well-known production of H_2O_2 in normal metabolism and the immune response.[36] Improving the low quantum yield and accelerating the kinetics are two ways to amplify this ultraweak CL for visible and functional light emission. The optical properties of metal nanomaterials dominated by localized surface plasmons are size and shape dependent.[37] Therefore, studying the effect of specifically designed ultrasmall metal nanoclusters on the ultraweak CL would provide new principles and applications of this CL system.

In this work, we synthesized zinc−copper bimetal nanoclusters using bovine serum albumin (BSA) by a simple chemical reduction method. BSA was used as the model protein for the synthesis and stabilization of zinc−copper bimetal nanoclusters. The as-prepared

Zn/Cu@BSA NCs exhibit bright, stable fluorescence and have excellent water dispersion property. The ultraweak CL from the decomposition of HCO_4^- in the $NaHCO_3-H_2O_2$ system was significantly enhanced by Zn/Cu@BSA NCs. The mechanism of the chemiluminescence was investigated. The structure change of BSA led to the formation of larger metal particles in the CL reaction. The amplified CL was induced from the catalysis of Zn/Cu@BSA NCs and the metal surface plasmon coupled emission of $(CO_2)_2^*$. This Zn/Cu@BSA NC-amplified CL system has been exploited for the highly sensitive and selective measurement of hydrogen peroxide in water samples in this study.

RESULTS AND DISCUSSION

Characterization of Zn/Cu@BSA NC. Figure 1a shows the absorption spectrum of Zn/Cu@BSA NCs and the absorbance maximum of Zn/Cu@BSA NCs located at 350 nm, while pure BSA had an absorption spectrum at 280 nm. The transmission electron microscopy (TEM) image of the as-prepared Zn/Cu@BSA NCs indicated that the average particle size was about 1.9 ± 0.2 nm. The fluorescence spectra of Zn/Cu@BSA NCs excited at 350 nm show that the emission intensity depends on the initial concentration of metal ions in the reactant, and at higher metal ion concentration diminution of emission occurs as nanoparticles are formed. Zn/Cu@BSA NCs prepared with a metal ion concentration of 2.0 mM generated the strongest emission at 430 nm and presented bright and blue emission under ultraviolet (UV) radiation (365 nm) (Figure 1b). X-ray photoelectron spectroscopy (XPS) analysis was carried out to determine the oxidation state of copper, zinc, and sulfur in the samples before and after the CL reaction. All expected elements appeared in the survey spectrum (Figure 2a). The $2p_{3/2}$ and $2p_{1/2}$ features of Cu(0) and Zn(0) are weaker in the Zn/Cu@BSA NCs (lines 1 in Figure 2b and c). However, when a Zn/Cu@BSA NC is added in the $NaHCO_3-H_2O_2$ CL system, two intense
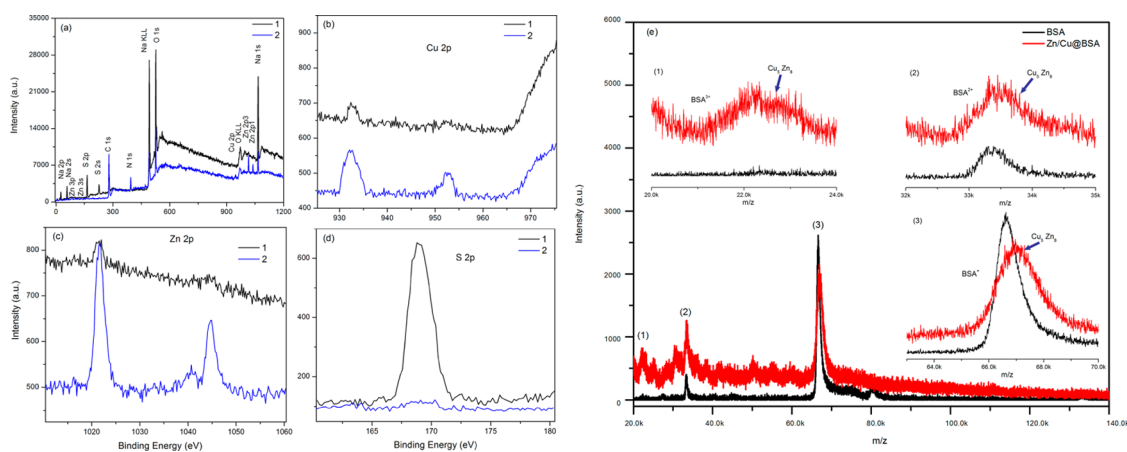
Figure 2. XPS spectra of Zn/Cu@BSA NCs obtained before (line 1) and after (line 2) CL reaction. (a) Survey of Zn/Cu@BSA NCs, (b) Cu_{2p}, (c) Zn_{2p}, (d) S_{2p}, and (e) MALDI-TOF mass spectra of BSA (black) and Zn/Cu@BSA NC (red). The peaks due to triply (1), doubly (2), and singly (3) charged ions of Zn/Cu@BSA NCs are expanded in the inset.

peaks are observed at 932.4 and 952.2 eV, which are assigned to $2p_{3/2}$ and $2p_{1/2}$ features of Cu(0) (Figure 2b, line 2), and two intense peaks are observed at 1021.45 and 1044.55 eV, which are assigned to $2p_{3/2}$ and $2p_{1/2}$ features of Zn(0), respectively (Figure 2c, line 2). This reveals that the metal NCs have changed their aggregation state after CL reaction. The single peak at 164.05 eV, which is assigned to 2p features of S(0), disappeared after the CL reaction, indicating the structure change of the protein (Figure 2d). Matrix-assisted laser desorption ionization time-of-flight (MALDI-TOF) mass spectrometry (MS) was used to study the number of copper and zinc atoms in the cluster core. The mass spectrum of BSA showed a major peak at around m/z 66 400 Da due to the monocation. The Zn/Cu NCs containing BSA showed a distinct, but low-intensity peak at m/z 67240 Da besides the parent protein peak. The difference between the above peaks and the host protein spectrum measured at pH 12 might be attributed to alloyed clusters containing 5 copper and 8 zinc atoms, *i.e.*, Cu_5Zn_8. The presence of doubly as well as triply charged clusters along with the corresponding peaks of the protein in the MALDI-TOF MS data clearly indicates that the Zn/Cu NC is associated with a single protein molecule. The aggregation of Cu_5Zn_8 clusters was further confirmed by powder X-ray diffraction (XRD) measurement. In the XRD patterns of Zn/Cu@BSA NCs (Figure S1, Supporting Information), the ultraweak and broad diffraction peaks of Cu_5Zn_8 (310), (222), and (330) could be identified.[38,39] Based on XPS, MALDI-TOF MS, and powder XRD data, we concluded that the copper−zinc nanoclusters were formed within BSA and are referred to as Zn/Cu@BSA NC henceforth.

Kinetic Aspects. The batch method was used to study the reaction of $NaHCO_3$, BSA, Zn/Cu@BSA NCs, and H_2O_2. The addition of Zn/Cu@BSA NCs or BSA to $NaHCO_3$ or H_2O_2 did not produce light. When Zn/Cu@BSA NCs were mixed with H_2O_2 first, and then

$NaHCO_3$ was injected, one CL peak was obtained. The CL intensity had a maximum value of 554 in 0.2 s, and the CL lasted for about 30 s (Figure 3a). When Zn/Cu@BSA NCs were mixed with $NaHCO_3$ first, then H_2O_2 was injected, a remarkable enhancement of CL was observed. The CL intensity reached 33 104 counts. The light lasted for about 150 s (Figure 3b). The effects of BSA, $CuSO_4$, and $Zn(NO_3)_2$ solutions on the CL of the $NaHCO_3$−H_2O_2 system are shown in Figure 3c. The above results indicate that BSA has no effect on the CL emission. Both $CuSO_4$ and $Zn(NO_3)_2$ solutions can change the CL kinetic curve. The CL intensity is enhanced about 3 times by $CuSO_4$ solution, and the intensity has no obvious change by the $Zn(NO_3)_2$ solution. These results indicate that the significantly enhanced CL in Figure 3b is related directly to Zn/Cu@BSA NCs.

The luminescence decay of the Zn/Cu@BSA NCs in water was measured by a picosecond-resolved time-correlated single photon counting (TCSPC) technique (Figure 4a). The decay profile of the Zn/Cu@BSA NCs was monitored at an excitation wavelength of 372 nm. The numerical fitting of the luminescence collected at 430 nm revealed time constants of 0.59, 2.60, and 15.12 ns, which might be due to the electronic transitions between the "sp" conduction band and the filled "d^{10}" band. The numerical fitting of the CL of the $NaHCO_3$−H_2O_2 system at the same condition revealed time constants of 0.64, 2.53, 15.59, and 171.04 ns. But when Zn/Cu@BSA NCs were added to the $NaHCO_3$−H_2O_2 system, the fitted time constants were 0.66, 2.54, and 13.32 ns. These changes in time constant indicate that Zn/Cu@BSA NCs have been involved in the CL reaction and the structure of metal nanoclusters has been affected. The amplified CL may be generated from the surface-plasmons-enhanced effect. The stopped-flow experiment of the CL of the $NaHCO_3$−Zn/Cu@BSA NC−H_2O_2 system in the first 0.5 s of reaction was recorded, as shown in Figure 4b.
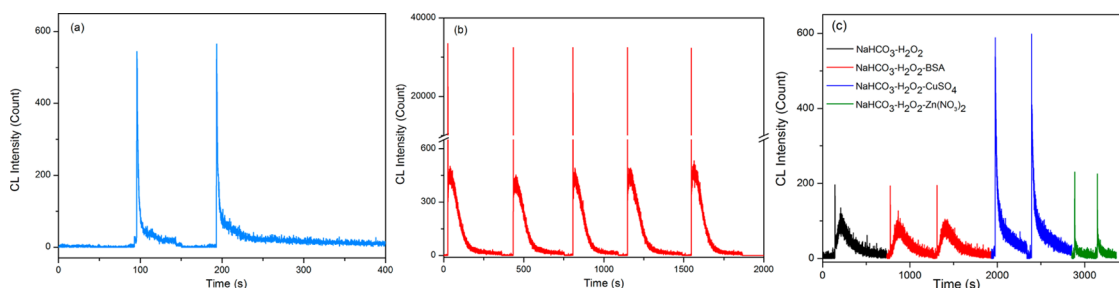
Figure 3. Kinetic curves of the NaHCO$_3$−Zn/Cu@BSA NC−H$_2$O$_2$ CL systems. (a) NaHCO$_3$ injected into a Zn/Cu@BSA NC−H$_2$O$_2$ solution, (b) H$_2$O$_2$ injected into a Zn/Cu@BSA NC−NaHCO$_3$ solution, and (c) effects of BSA, CuSO$_4$, and Zn(NO$_3$)$_2$ on the NaHCO$_3$−H$_2$O$_2$ CL system. Solution conditions were 0.2 M NaHCO$_3$, 0.1 M H$_2$O$_2$, 2.0 mM Zn/Cu@BSA NCs, 2.0 mM CuSO$_4$, and 2.0 mM Zn(NO$_3$)$_2$.
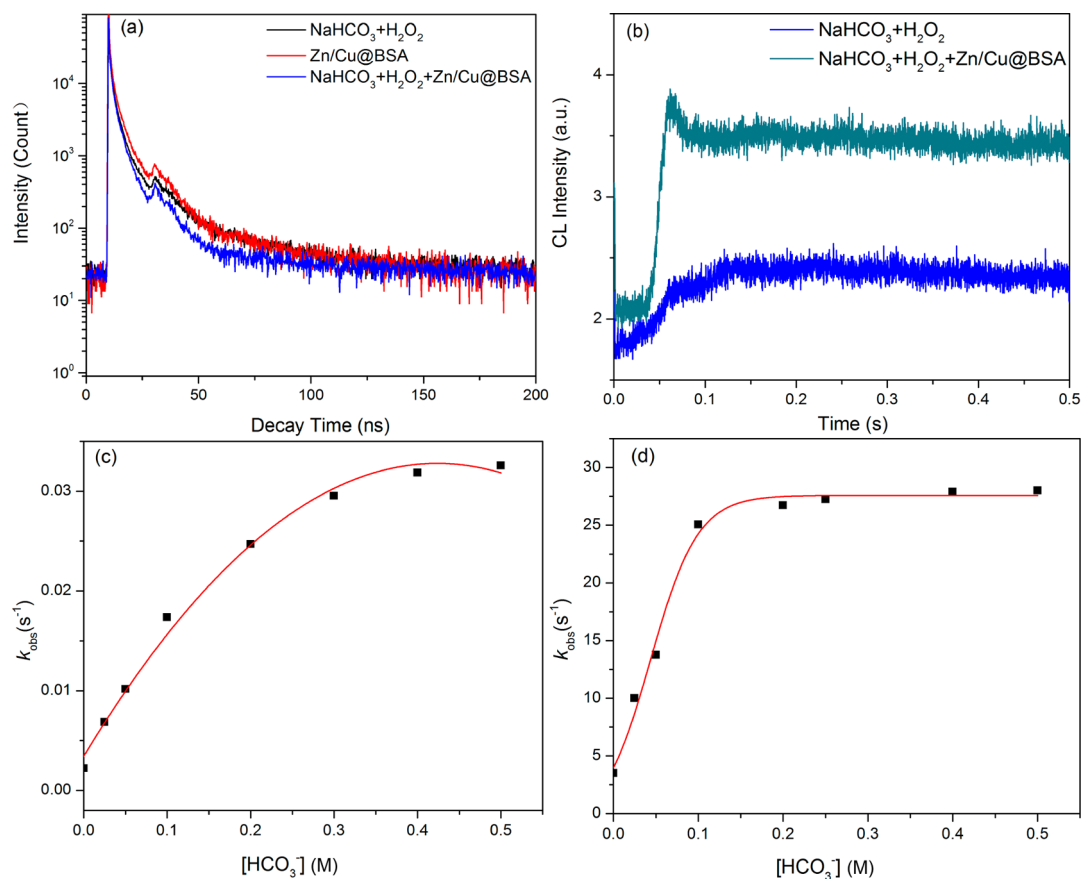

Figure 4. Kinetics of fluorescence decay and CL reaction. (a) Lifetime profiles of Zn/Cu@BSA NCs and Zn/Cu@BSA NCs in the NaHCO$_3$−H$_2$O$_2$ system, (b) stopped-flow kinetic curves of the NaHCO$_3$−H$_2$O$_2$ system with and without Zn/Cu@BSA NCs in 0.5 s, (c) dependence of the rate constant on [HCO$_3^-$] for CL at pH 11.80 in the NaHCO$_3$−H$_2$O$_2$ system, and (d) that in the NaHCO$_3$−Zn/Cu@BSA NC−H$_2$O$_2$ system.

The rate of CL was accelerated in the presence of Zn/Cu@BSA NCs, and the equilibrium amount of HCO$_4^-$ decreased. The calculated second-order rate constant obtained by using a nonlinear regression from the plot of the experimental observed rate constant k_{obs} versus [H$_3$O$^+$] with increasing amounts of [HCO$_3^-$] is approximately 100-fold greater than that of the NaHCO$_3$−H$_2$O$_2$ system without Zn/Cu@BSA NCs (Figure 4c and d).

Spectra of CL Systems. To further verify the possible mechanism of the amplified CL, the UV−vis absorption spectrum change of Zn/Cu@BSA NCs was investigated.

When Zn/Cu@BSA NC was added to the NaHCO$_3$−H$_2$O$_2$ system, two obvious absorption peaks at 440 and 650 nm were observed, and the absorbance was increased during the first 5 min of reaction. The absorption peaks of BSA and Zn/Cu@BSA NCs at 280 and 350 nm disappeared. This indicated that the structure of BSA had been changed by a redox reaction, which further caused the aggregation of Zn/Cu@BSA NCs to larger metal particles. The observed peaks were assigned to the surface plasmon absorption of the formed Zn/Cu NPs (Figure 5a).[28]
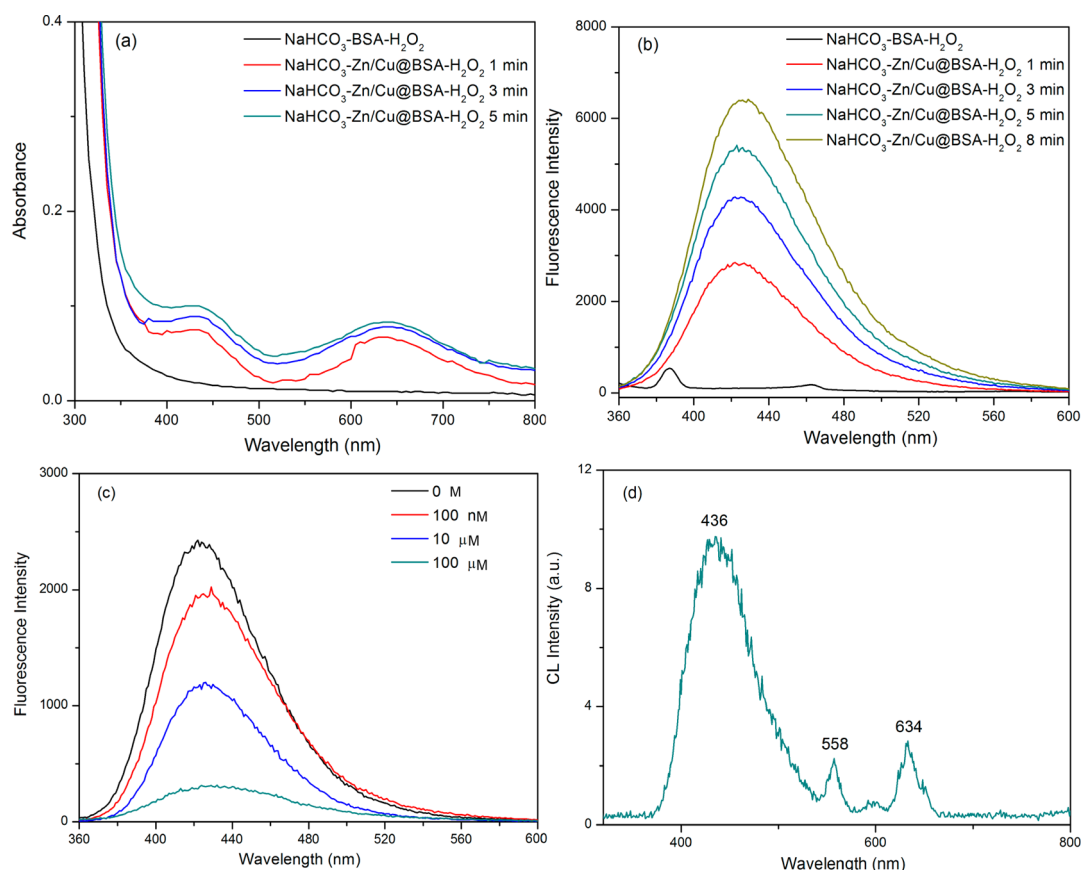
Figure 5. Spectra of Zn/Cu@BSA NCs. (a) UV−vis absorption spectra of Zn/Cu@BSA NCs in the NaHCO$_3$−H$_2$O$_2$ system, **(b)** fluorescence spectra of the NaHCO$_3$−H$_2$O$_2$ system with Zn/Cu@BSA NCs at different reaction times (λ_{ex} = 350 nm), **(c)** fluorescence spectra of Zn/Cu@BSA NCs with the addition of H$_2$O$_2$ (0−100 μM) (λ_{ex} = 350 nm), and **(d)** the CL spectra of the NaHCO$_3$−Zn/Cu@BSA NC−H$_2$O$_2$ system. Solution conditions were 0.2 M NaHCO$_3$, 0.1 M H$_2$O$_2$, and 2.0 mM Zn/Cu@BSA NCs. The flow rate was 1.0, 1.0, and 1.5 mL min^{-1} for Zn/Cu@BSA NCs, NaHCO$_3$, and H$_2$O$_2$, respectively.

The fluorescence emission of this CL system with Zn/Cu@BSA NCs during the first 8 min of reaction is shown in Figure 5b. The maximum emission was located at 435 nm, the fluorescence intensity increased, and the maximum emission shifted to the red with an increase in reaction time. Under the same conditions, the maximum emission of the NaHCO$_3$−BSA−H$_2$O$_2$ system was located at 385 nm, and the sharp peak was the Raman peak of water. The weaker emission at 461 nm from BSA indicated that the contributor of emission from BSA can be neglected under these conditions. The increasing fluorescence emission of the NaHCO$_3$−Zn/Cu@BSA NC−H$_2$O$_2$ system is related to the surface plasmons of the metal nanoparticles. Figure 5c shows the effect of 0−100 μM H$_2$O$_2$ on the fluorescence of Zn/Cu@BSA NCs. The emission decreased with increasing concentration of H$_2$O$_2$. It further indicates that H$_2$O$_2$ has an effect on the structure change of BSA, and it accelerates the aggregation of metal, causing fluorescence quenching. This result further proved that the increasing emission in Figure 5b was from the surface plasmon enhancement.

CL spectra were measured to identify the emitting species. Three peaks in the range 300−800 nm are observed in the CL spectrum of the NaHCO$_3$−Zn/Cu@BSA NC−H$_2$O$_2$ system (Figure 5d). The peak at 436 nm corresponds to the decomposition of excited double (CO$_2$)$_2$*.[40,41] The peak at 634 nm results from the emission of ^{1}O$_2$.[42] The peak at 558 nm is a new emission species compared with those reported in the NaHCO$_3$−H$_2$O$_2$ CL system. They may result from the emission of any tryptophan metabolites.[28]

A circular dichroism (CD) spectrum has been employed to study the conformational behavior of BSA in Zn/Cu@BSA NC before and after CL reaction. Native BSA displays CD features with minima at 208 and 222 nm, corresponding to the secondary structure of the protein. However, after the formation of Zn/Cu@BSA NCs, the 208 nm peak is shifted to 204 nm, indicating the loss of α-helix content and increase in β-sheet and random coil structures (Figure 6a).[43] The percentage of various conformations has been determined for both pure BSA and Zn/Cu@BSA NCs by using CDNN software, which revealed 51% loss of α-helix structure. After CL reaction, about 71.2% loss of α-helix structure, 16.8% addition of β-sheet structure, and 18.6% addition of random coil structure were observed. The structure change process of Zn/Cu@BSA
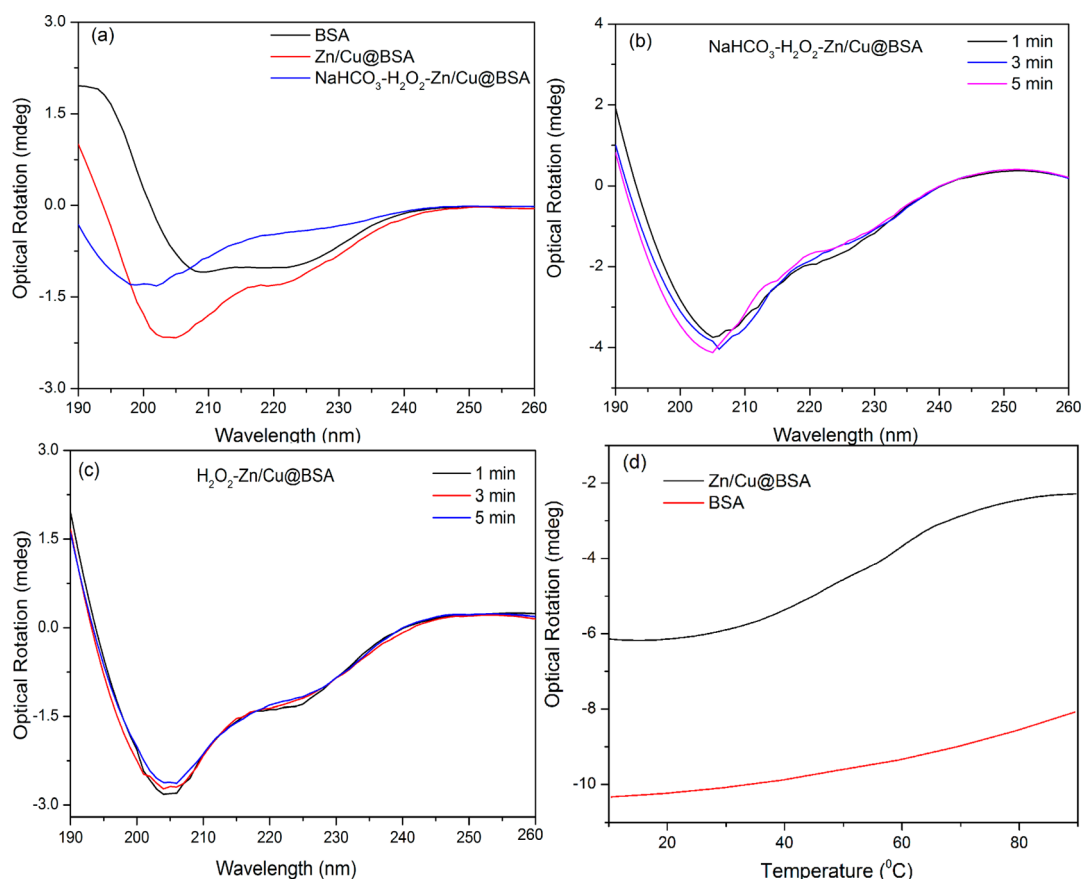
Figure 6. CD spectrum for the secondary structure of protein in Zn/Cu@BSA NCs. (a) Far-UV CD spectra of BSA (black), Zn/Cu@BSA NC (red), and Zn/Cu@BSA NCs in the NaHCO$_3$–H$_2$O$_2$ system (blue), (b) the change of CD spectra of Zn/Cu@BSA NCs in the NaHCO$_3$–H$_2$O$_2$ system and (c) in H$_2$O$_2$ solution, and (d) the CD change of Zn/Cu@BSA NCs (black) and BSA (red) at different temperatures.

NCs in the NaHCO$_3$–H$_2$O$_2$ system and in H$_2$O$_2$ solution is shown in Figure 6b and c, respectively. It indicated that the structure change of Zn/Cu@BSA NCs occurred easily during the first 5 min of CL reaction. The structure change of Zn/Cu@BSA NCs was also easily affected by temperature, as shown in Figure 6d.

Spin-Trapping Studies. Room-temperature electron spin resonance (ESR) spectroscopy was employed to confirm the existence of $^1O_2$ and ·OH radicals. 2,2,6,6-Tetramethyl-4-piperidine (TEMP) can react with $^1O_2$ to give the TEMPO adduct, which is a stable nitroxide radical with a characteristic spectrum.[44] Figure 7a shows the specific signal of TEMPO in the NaHCO$_3$–H$_2$O$_2$ system, which confirmed that $^1O_2$ was generated in the system. Figure 7b shows the intensity change of TEMPO in the NaHCO$_3$–Zn/Cu@BSA NC–H$_2$O$_2$ system. The increasing intensity of TEMPO supported the constant formation of $^1O_2$ in the NaHCO$_3$–Zn/Cu@BSA NC–H$_2$O$_2$ system in the first 26 min of the reaction.

5,5-Dimethyl-1-pyrroline N-oxide (DMPO) was used as the radical trapper to detect ·OH and ·CO$_3^-$ by forming the DMPO–OH adduct in the ESR experiment. Figure 7c presents the formation of ·OH and ·CO$_3^-$ radicals in the NaHCO$_3$–H$_2$O$_2$ system and the

decreasing signal during the first 10 min of reaction. Figure 7d shows the signal change of the DMPO–OH adduct in the first 18 min of reaction in the NaHCO$_3$–Zn/Cu@BSA NC–H$_2$O$_2$ system. The results confirmed the generation of ·OH and ·CO$_3^-$ radicals in the NaHCO$_3$–Zn/Cu@BSA NC–H$_2$O$_2$ system. Figure 7e further indicates that ·OH exists and the reaction of Zn/Cu@BSA NCs affects its lifetime. ESR is very effective at probing subtle changes in the structure and surrounding environments of radicals and magnetic ions. Subtle changes in structure lead to shifts in the g factor.[45−47] Figure 7f shows the change in g value of Zn/Cu@BSA NCs in a H$_2$O$_2$ solution and the NaHCO$_3$–H$_2$O$_2$ system. It further proves the structure change of Zn/Cu@BSA NCs in the CL reaction.

Mechanism of the CL Reaction. On the basis of the ESR results, UV–vis absorption spectra, fluorescence spectra, and CL spectra of the NaHCO$_3$–Zn/Cu@BSA NC–H$_2$O$_2$ system, the CL mechanism is proposed as further shown in Figure 8. First, HCO$_4^-$ formed from the reaction between H$_2$O$_2$ and NaHCO$_3$ (reaction 1).[48]

$$HCO_3^- + H_2O_2 \rightleftharpoons HCO_4^- + H_2O \qquad (1)$$

The active sites of the prepared Zn/Cu@BSA NCs facilitate the decomposition of HCO$_4^-$ to generate the
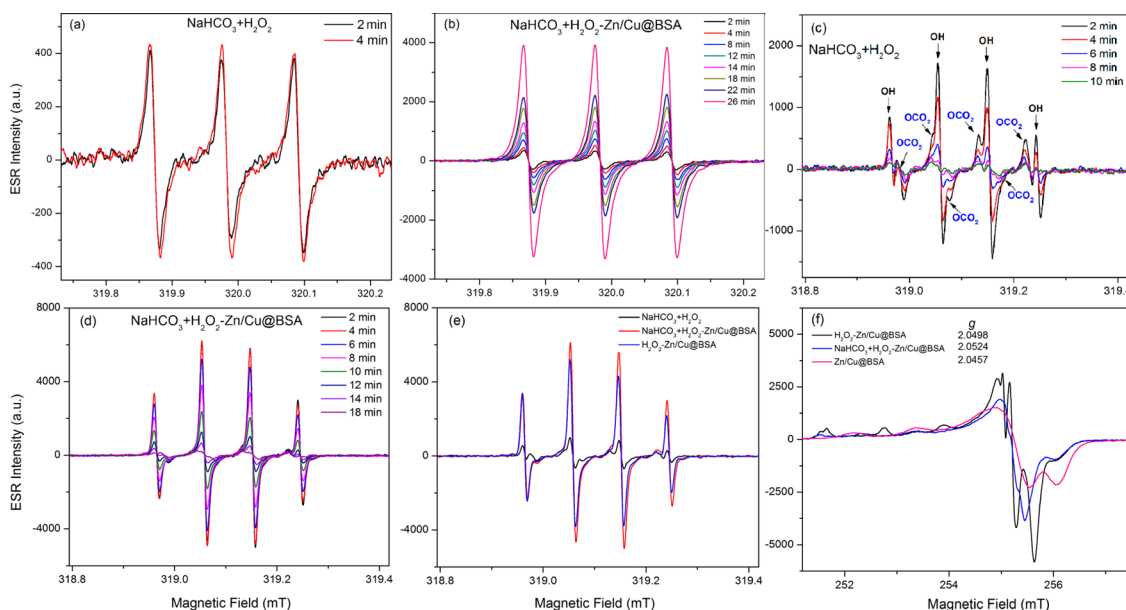
Figure 7. ESR spectra of $^1O_2$ and $\cdot OH$ radicals. (a) $^1O_2$ produced in the $NaHCO_3-H_2O_2$ system and (b) in the $NaHCO_3-Zn/Cu@BSA$ NC$-H_2O_2$ system, (c) $\cdot OH$ produced in the $NaHCO_3-H_2O_2$ system and (d) in the $NaHCO_3-Zn/Cu@BSA$ NC-H_2O_2 system, (e) the signal change of $\cdot OH$ in H_2O_2 solution and the $NaHCO_3-H_2O_2$ system, and (f) the change in g factor of Zn/Cu@BSA NCs in H_2O_2 solution and the $NaHCO_3-H_2O_2$ system. Experimental conditions: 0.05 M TEMP, 0.05 M DMPO, 0.2 M $NaHCO_3$, 0.1 M H_2O_2, and 2.0 mM Zn/Cu@BSA NCs.
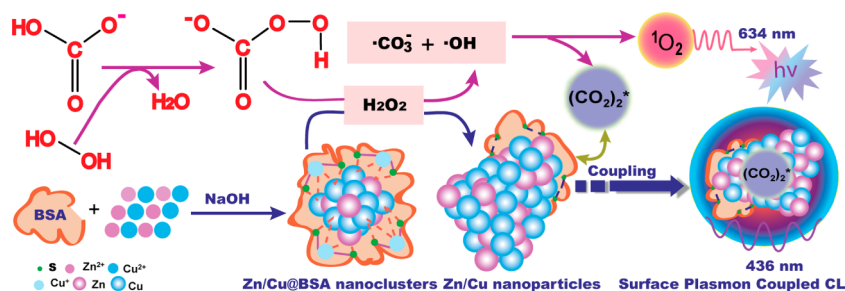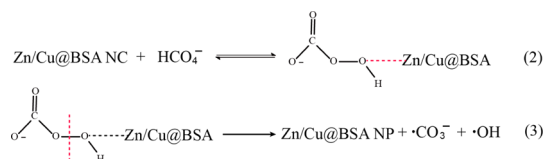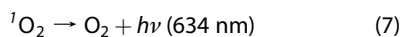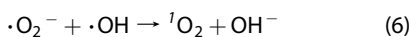

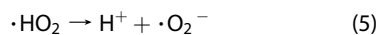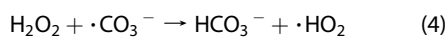**Figure 8.** Schematic illustration of the CL mechanism of the $NaHCO_3-Zn/Cu@BSA$ NC$-H_2O_2$ system.

key intermediate radicals, $\cdot OH$ and $\cdot CO_3^-$, by catalysis (reactions 2 and 3).[49]

$$\text{(2)}$$

$$\text{(3)}$$

$\cdot OH$ and $\cdot CO_3^-$ radicals will react with H_2O_2 to form emitter intermediate $^1O_2$ (reactions 4-7), which has been confirmed by a CL spectrum in Figure 5d and an ESR experiment in Figure 7b.[50]

$$H_2O_2 + \cdot CO_3^- \rightarrow HCO_3^- + \cdot HO_2 \qquad (4)$$

$$\cdot HO_2 \rightarrow H^+ + \cdot O_2^- \qquad (5)$$

$$\cdot O_2^- + \cdot OH \rightarrow {}^1O_2 + OH^- \qquad (6)$$

$$^1O_2 \rightarrow O_2 + h\nu \text{ (634 nm)} \qquad (7)$$

Simultaneously, $\cdot OH$ will react with excess HCO_3^-, forming emitter intermediate $(CO_2)_2^*$, which is unstable and decomposes to CO_2, releasing energy to generate light at 430-460 nm (reactions 8-10).[51,52] This is consistent with the CL spectrum of the $NaHCO_3-Zn/Cu@BSA$ NC$-H_2O_2$ system.

$$\cdot OH + HCO_3^- \rightarrow OH^- + \cdot HCO_3 \qquad (8)$$

$$2\cdot HCO_3 \rightarrow (CO_2)_2^* + H_2O_2 \qquad (9)$$

$$(CO_2)_2^* \rightarrow 2CO_2 + h\nu \text{ (436 nm)} \qquad (10)$$
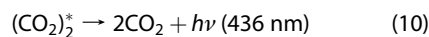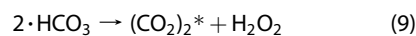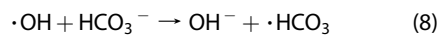
Considering the structure of Zn/Cu@BSA NCs, the thiol group of cysteine residues in BSA played an important role as the stabilizer for the nanoclusters. It has been reported that the Au$-$S bond can be degraded in the presence of H_2O_2 as an oxidant.[53] Disulfides and sulfonates are not chemisorbed and, therefore, can be easily removed from the Zn/Cu surface. Thus, these reactions could lead to a rapid deterioration of structure of Zn/Cu NCs.

The transformation of metal NCs to the large size of Zn/Cu NPs also was confirmed from the recorded TEM images. As shown in Figure 9, the average sizes of Zn/Cu NPs were 3.8 ± 0.3 and 6.6 ± 0.4 nm when Zn/Cu NCs were added to 0.1 M H_2O_2 and the mixing solution of 0.2 M $NaHCO_3$ and 0.1 M H_2O_2, respectively. It can be observed from TEM images that the BSA scaffolds seen clearly around the Zn/Cu NCs gradually disappeared after the chemical reactions. High-resolution TEM images of Zn/Cu@BSA NCs before and after CL reaction further proved the structure change from nanoclusters to polycrystalline nanoparticles (Figure S2, Supporting Information). Since the wavelength of CL emission and the surface plasmons of Zn/Cu NPs overlapped, the emission from $(CO_2)_2^*$ was readily induced/coupled to surface plasmons, amplifying the CL signal (reactions 11−13).

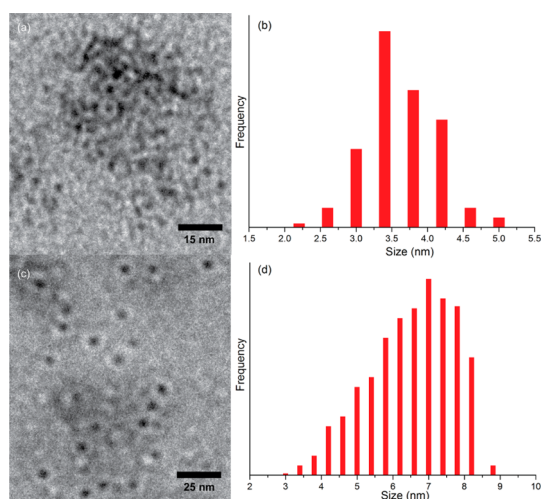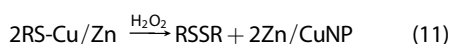$$2RS\text{-}Cu/Zn \xrightarrow{H_2O_2} RSSR + 2Zn/CuNP \qquad (11)$$

Figure 9. TEM images and size distribution analysis of Zn/Cu@BSA NCs in the presence of H_2O_2 (a, b, 3.8 ± 0.3 nm) and the mixing solution of $NaHCO_3$−H_2O_2 (c, d, 6.6 ± 0.4 nm), respectively; 200 particles are measured to obtain the size distribution.

$$(CO_2)_2^* + Zn/CuNP \rightarrow Zn/CuNP\text{-}(CO_2)_2^* \qquad (12)$$

$$Zn/CuNP\text{-}(CO_2)_2^* \rightarrow Zn/CuNP + 2CO_2 + h\nu \text{ (436 nm)} \qquad (13)$$

Application of the CL System. The $NaHCO_3$−Zn/Cu@BSA NC−H_2O_2 CL system was developed as a flow injection analysis (FIA) system for H_2O_2 sensoring (Figure S3, Supporting Information). The effects of several physicochemical parameters, such as the concentration of reagent, pH, and the flow rate, on the FIA sensing system were optimized. A 2.0 mM Zn/Cu@BSA NC solution diluted 500 times before reaction and 0.2 M $NaHCO_3$ were selected (Figure S4a, Supporting Information). The CL intensity increased with increasing pH and reached a maximum at pH 11.80. Therefore, pH 11.80 was selected in the $NaHCO_3$−Zn/Cu@BSA NC−H_2O_2 system (Figure S4b, Supporting Information). The optimal flow rate of the carrier, $NaHCO_3$, and Zn/Cu@BSA NCs was 1.5, 1.0, and 1.0 mL min^{-1} considering both analytical precision and solution consumption.

The FIA CL signal for H_2O_2 with sharp peaks and low noise and the calibration plot are shown in Figure 10a. Under the optimized conditions, the limit of detection for H_2O_2 was 3.0×10^{-10} M (S/N = 3). The calibration plot showed a good linear relationship between the CL intensity and the H_2O_2 concentration in the range from 5.0×10^{-9} to 1.0×10^{-6} M with a correlation coefficient of 0.9998 (Figure 10b). The relative standard deviation (RSD) for 10 parallel measurements (intra-assay) of 0.5 μM H_2O_2 was 2.1%. The RSD for five parallel measurements (interassay) of 0.5 μM H_2O_2 using five different batches of Zn/Cu@BSA NCs was 6.8%. The RSD of the reproducibility of Zn/Cu@BSA NCs in two months was 3.7%. In addition, the detection limit of this Zn/Cu@BSA NC-enhanced CL sensor for H_2O_2 has been compared with that of a fluorescent
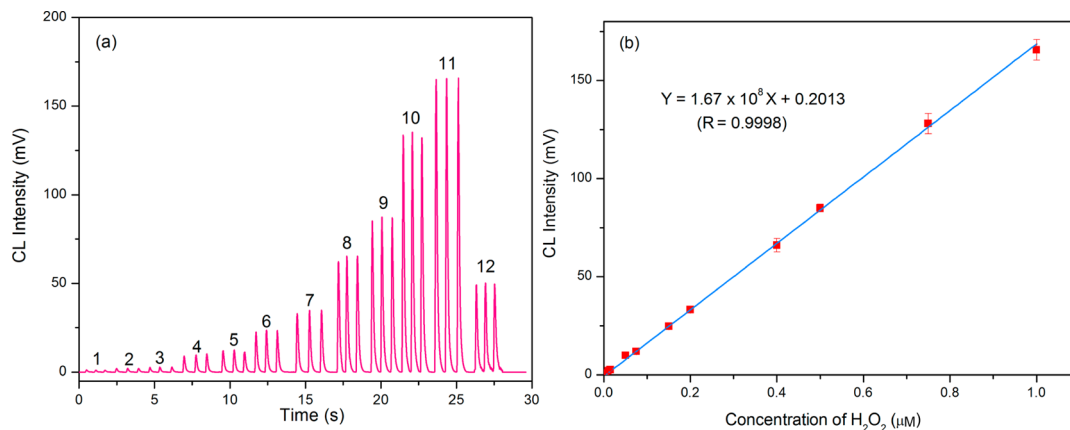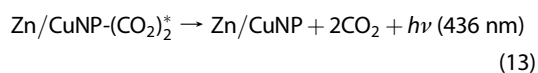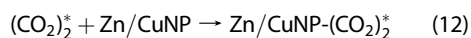

Figure 10. FIA-CL signals and the intensity. (a) Typical FIA-CL signals for H_2O_2, concentration of H_2O_2 (μM) (1) 0.005; (2) 0.01; (3) 0.015; (4) 0.05; (5) 0.075; (6) 0.15; (7) 0.2; (8) 0.4; (9) 0.5; (10) 0.75; (11) 1.0; (12) sample; and (b) linear calibration plot of the CL reaction for H_2O_2.

gold nanocluster sensor. The CL sensor exhibits better performance than that fluorescent one with a detection limit of 30 nM.[23] These results indicated that the proposed CL sensor has good linearity and relatively high sensitivity and precision.

The effect of coexisting ions in water on the sensing of 0.5 μM H_2O_2 was also investigated in this study. The tolerance limit was estimated with a $\pm$5% relative error in peak height. Many ions have no influence at concentrations below 1.0×10^{-4} M. Uric acid, dopamine, D-glucose, glutathione, and ascorbic acid have no effects on CL at concentrations below 1.0×10^{-5} M. Other substances, such as 50-fold Zn^{2+}, Al^{3+}, Ca^{2+}, Mg^{2+}, Fe^{2+}, and Fe^{3+}, 20-fold Cu^{2+}, 500-fold CH_3COO^-, BSA, EDTA, and 1000-fold K^+, Na^+, NO_3^-, Cl^-, and SO_4^{2-} have no effects on the detection of 0.5 μM H_2O_2. These data demonstrated that the developed sensor has a high selectivity for H_2O_2.

The proposed CL sensor has been applied for H_2O_2 in water samples. Freshly collected water samples were filtrated by a 0.22 μm microfilm and spiked with 1.0×10^{-5} M EDTA as a masking reagent for transition metals before determination. Recovery test and method comparison were performed to evaluate the accuracy and reliability of the sensor. The recoveries for the samples were in the range 90−103% (Table S1, Supporting Information). Moreover, the sensing results were in good agreement with another reported method,[54] indicating the application was comparable and acceptable.

CONCLUSIONS

In summary, Zn/Cu@BSA NCs with excellent optical properties have been successfully synthesized using BSA as a capping protein. Zn/Cu@BSA NCs catalyzed the decomposition of HCO_4^- with structure change of the protein, which led to the aggregation of metal nanoclusters to metal nanoparticles. Simultaneously, the coupling of excited $(CO_2)_2$ to surface plasmons of Zn/Cu NPs further amplified the CL. As a result, a strong CL was observed in the $NaHCO_3$−Zn/Cu@BSA NC−H_2O_2 system. The optimized CL system with metal nanoclusters can be used as a sensor for H_2O_2 in water samples with high sensitivity and good recovery.

EXPERIMENTAL SECTION

Chemicals. Hydrogen peroxide (30%, Alfa Aesar), sodium hydrogen carbonate, zinc nitrate, copper sulfate (>99.9%, Beijing Chemical Reagent), bovine serum albumin (>99%, Amresco), 5,5-dimethyl-1-pyrroline N-oxide (>99.9%, Tokyo Kasei Kogyo), and 2,2,6,6-tetramethyl-4-piperidine (>99.9%, Sigma-Aldrich) were used. All water used was ultrapure (18.3 M$\Omega\cdot$cm).

Apparatus. Batch CL experiments were carried out with a BPCL luminescence analyzer (Institute of Biophysics, Chinese Academy of Sciences, Beijing, China). Absorption spectra were collected using a UV-3900 UV−vis spectrophotometer (Hitachi, Tokyo, Japan). Emission spectra were measured with an F-7000 fluorescence spectrophotometer (Hitachi, Tokyo, Japan). The width of the excitation slit and emission slit were both set as 10 nm, and PMT detector voltage was selected high at 800 V for the measurement of all fluorescence spectra. ESR spectra were measured on a model JES-FA200 spectrometer (JEOL, Tokyo, Japan). The XPS was carried out on a PHI Quantera SXM spectrometer with an Al Kα X-ray source (ULVAC-PHI, Chigasaki, Japan). Powder XRD data were collected using a Bruker D8 X-ray diffractometer with Cu Kα radiation at 40 kV and 40 mA (Bruker, Karlsruhe, Germany). Transient fluorescence decays were detected with an Edinburgh Instruments LP 920 spectrometer with the TCSPC technique (Edinburgh, Livingston, U.K.). CD measurement was performed on a Pistar π-180 Chirascan CD spectrophotometer, and the reaction rate of chemiluminescence was monitored in an SX 20 stopped-flow spectrophotometer (Applied Photophysics, Leatherhead, U.K.). TEM image was recorded on a FEI Tecnai G2 F20 S-Twin microscope with an accelerating voltage of 200 kV (FEI, OR, USA). The mass spectrum was obtained by a Bruker Autoflex MALDI-TOF mass spectrometer (Bruker Daltonics, MA, USA). Sinapinic acid was used as the matrix.

Synthesis of Zn/Cu@BSA NCs. Aqueous $Zn(NO_3)_2$ solution (0.5 mL, 2.0 mM) and $CuSO_4$ solution (0.5 mL, 2.0 mM) were added to a BSA solution (5 mL, 15 mg mL^{-1}). The solution was stirred at room temperature for about 5 min, and then a NaOH solution was introduced to adjust the pH to about 12. The color of the solution changed from blue to violet within 3−5 min. Finally, the mixture was allowed to stir at 55 °C for about 8 h, and the color changed to light brown.

$NaHCO_3$−Zn/Cu@BSA NC−H_2O_2 CL System. The light-producing reaction was carried out in a glass cuvette under ambient conditions by a batch method, and the detection was performed on a BPCL luminescence analyzer. First, 100 μL of 0.2 M $NaHCO_3$ and 50 μL of Zn/Cu@BSA NCs were mixed in a glass cuvette, and then 100 μL of 0.1 M H_2O_2 solution was injected by a microliter syringe. The CL intensity was displayed and integrated with 0.1 s intervals at 1.2 kV.

CL Spectral Measurements. The CL spectrum was obtained with a Hitachi F-7000 spectrophotometer when the Xe lamp was turned off with a flow analysis apparatus, which consisted of two peristaltic pumps, a CL detector, and a flow cell placed inside the cell holder of the fluorescence spectrophotometer. The emission slit width was opened to 20 nm during the recording of the CL spectrum. All optical measurements were performed at room temperature.

Kinetic Studies. The rate of HCO_4^- formation in the presence of Zn/Cu@BSA NCs was monitored from the loss of hydrogen peroxide absorbance at 240 nm in a stopped flow spectrophotometer ($\varepsilon_{240\ nm}$ = 43.6 M^{-1} cm^{-1}). Pre-equilibrium formation of HCO_4^- was assumed, whose concentration was maintained at steady state. The pseudophase model was employed to fit the kinetic data.

ESR Experiments. ESR spectra were recorded at room temperature using a JEOL JES-FA200 spectrometer. For the examination of $^1O_2$ (or ·OH radicals), first, 10 μL of $NaHCO_3$ (0.2 M) was mixed with 10 μL of Zn/Cu@BSA NCs (2.0 mM); then 30 μL of 0.05 M DMPO (or 0.05 M TEMP) was added. Finally, 10 μL of H_2O_2 (0.1 M) was injected into the above mixed solution. In a typical experiment, a final volume of 10 μL of this sample solution was loaded into a 50 μL quartz micropipette for the ESR measurement. All spectra were recorded at the appropriate time after the addition of the oxidant. Instrumental conditions: microwave power, 1.0 mW; modulation amplitude, 1.0 G; and receiver gain, 1.00e + 05.

Conflict of Interest: The authors declare no competing financial interest.

Supporting Information Available: The powder XRD patterns of Zn/Cu@BSA NCs, high-resolution TEM images of Zn/Cu@BSA NCs before and after the CL reaction, schematic diagram of the flow injection CL sensing system, effects of different

concentrations of reagents and pH on the CL intensity in FIA, results of H_2O_2 sensing and recoveries in water samples. This material is available free of charge *via* the Internet at http://pubs.acs.org.

REFERENCES AND NOTES

1. Zheng, J.; Nicovich, P. R.; Dickson, R. M. Highly Fluorescent Noble-Metal Quantum Dots. *Annu. Rev. Phys. Chem.* **2007**, *58*, 409–431.

2. Luo, Z.; Zheng, K.; Xie, J. Engineering Ultrasmall Water-Soluble Gold and Silver Nanoclusters for Biomedical Applications. *Chem. Commun.* **2014**, *50*, 5143–5155.

3. Goswami, N.; Zheng, K.; Xie, J. Bio-NCs-the Marriage of Ultrasmall Metal Nanoclusters with Biomolecules. *Nanoscale* **2014**, *6*, 13328–13347.

4. Qian, M.; Reber, A. C.; Ugrinov, A.; Chaki, N. K.; Mandal, S.; Saavedra, H. M.; Khanna, S. N.; Sen, A.; Weiss, P. S. Cluster-Assembled Materials: Toward Nanomaterials with Precise Control over Properties. *ACS Nano* **2010**, *4*, 235–240.

5. Mostafavi, M.; Keghouche, N.; Delcourt, M. O.; Belloni, J. Ultra-Slow Aggregation Process for Silver Clusters of a Few Atoms in Solution. *Chem. Phys. Lett.* **1990**, *167*, 193–197.

6. Zeng, C.; Liu, C.; Chen, Y.; Rosi, N. L.; Jin, R. Gold-Thiolate Ring as a Protecting Motif in the $Au_{20}(SR)_{16}$ Nanocluster and Implications. *J. Am. Chem. Soc.* **2014**, *136*, 11922–11925.

7. Zhou, Z.; Dong, S. Protein-DNA Interactions: A Novel Approach to Improve the Fluorescence Stability of DNA/Ag Nanoclusters. *Nanoscale* **2015**, *7*, 1296–1300.

8. Choi, S.; Dickson, R. M.; Yu, J. Developing Luminescent Silver Nanodots for Biological Applications. *Chem. Soc. Rev.* **2012**, *41*, 1867–1891.

9. Jia, X.; Li, J.; Wang, E. Supramolecular Self-Assembly of Morphologydependent Luminescent Ag Nanoclusters. *Chem. Commun.* **2014**, *50*, 9565–9568.

10. Zeng, C.; Chen, Y.; Li, G.; Jin, R. Magic Size $Au_{64}(S\text{-}c\text{-}C_6H_{11})_{32}$ Nanocluster Protected by Cyclohexanethiolate. *Chem. Mater.* **2014**, *26*, 2635–2641.

11. Wen, Q.; Gu, Y.; Tang, L.; Yu, R.-Q.; Jiang, J.-H. Peptide-Templated Gold Nanocluster Beacon as a Sensitive, Label-Free Sensor for Protein Post-translational Modification Enzymes. *Anal. Chem.* **2013**, *85*, 11681–11685.

12. Enkin, N.; Wang, F.; Sharon, E.; Albada, H. B.; Willner, I. Multiplexed Analysis of Genes Using Nucleic Acid-Stabilized Silver-Nanocluster Quantum Dots. *ACS Nano* **2014**, *8*, 11666–11673.

13. Yuan, Z.; Chen, Y.-C.; Li, H.-W.; Chang, H.-T. Fluorescent Silver Nanoclusters Stabilized by DNA Scaffolds. *Chem. Commun.* **2014**, *50*, 9800–9815.

14. Yin, J.; He, X.; Wang, K.; Xu, F.; Shangguan, J.; He, D.; Shi, H. Label-Free and Turn-on Aptamer Strategy for Cancer Cells Detection based on a DNA-Silver Nanocluster Fluorescence upon Recognition-Induced Hybridization. *Anal. Chem.* **2013**, *85*, 12011–12019.

15. Dainese, T.; Antonello, S.; Gascón, J. A.; Pan, F.; Perera, N. V.; Ruzzi, M.; Venzo, A.; Zoleo, A.; Rissanen, K.; Maran, F. $Au_{25}(SEt)_{18}$, a Nearly Naked Thiolate-Protected Au_{25} Cluster: Structural Analysis by Single Crystal X-ray Crystallography and Electron Nuclear Double Resonance. *ACS Nano* **2014**, *8*, 3904–3912.

16. Sun, J.; Wu, H.; Jin, Y. Synthesis of Thiolated Ag/Au Bimetallic Nanoclusters Exhibiting an Anti-Galvanic Reduction Mechanism and Composition-Dependent Fluorescence. *Nanoscale* **2014**, *6*, 5449–5457.

17. Xie, J. P.; Zheng, Y. G.; Ying, J. Y. *J. Am. Chem. Soc.* **2009**, *131*, 888–889.

18. Xu, Y.; Sherwood, J.; Qin, Y.; Crowley, D.; Bonizzoni, M.; Bao, Y. The Role of Protein Characteristics in the Formation and Fluorescence of Au Nanoclusters. *Nanoscale* **2014**, *6*, 1515–1524.

19. Yu, Y.; New, S. Y.; Xie, J.; Su, X.; Tan, Y. N. Protein-Based Fluorescent Metal Nanoclusters for Small Molecular Drug Screening. *Chem. Commun.* **2014**, *50*, 13805–13808.

20. Choi, S.; Dickson, R. M.; Lee, J. K.; Yu, J. Generation of Luminescent Noble Metal Nanodots in Cell Matrices. *Photochem. Photobiol. Sci.* **2012**, *11*, 274–278.

21. Yu, J.; Choi, S.; Dickson, R. M. Shuttle-Based Fluorogenic Silver-Cluster Biolabels. *Angew. Chem., Int. Ed.* **2009**, *48*, 318–320.

22. Liu, X.; Wang, F.; Niazov-Elkan, A.; Guo, W.; Willner, I. Probing Biocatalytic Transformations with Luminescent DNA/Silver Nanoclusters. *Nano Lett.* **2013**, *13*, 309–314.

23. Wen, F.; Dong, Y.; Feng, L.; Wang, S.; Zhang, S.; Zhang, X. Horseradish Peroxidase Functionalized Fluorescent Gold Nanoclusters for Hydrogen Peroxide Sensing. *Anal. Chem.* **2011**, *83*, 1193–1196.

24. Chen, Z.; Luo, D.; Kang, M.; Lin, Z. New Semiconducting Coordination Polymers from Zinc Sulfide Clusters and Chains. *Inorg. Chem.* **2011**, *50*, 4674–4676.

25. Wei, W. T.; Lu, Y. Z.; Chen, W.; Chen, S. W. One-Pot Synthesis, Photoluminescence, and Electrocatalytic Properties of Subnanometer-Sized Copper Clusters. *J. Am. Chem. Soc.* **2011**, *133*, 2060–2063.

26. Jia, X.; Yang, X.; Li, J.; Li, D.; Wang, E. Stable Cu Nanoclusters: From an Aggregation-Induced Emission Mechanism to Biosensing and Catalytic Applications. *Chem. Commun.* **2014**, *50*, 237–239.

27. Sarkar, B.; Pendem, C.; Konathala, L. N. S.; Tiwari, R.; Sasakib, T.; Bal, R. Cu Nanoclusters Supported on Nanocrystalline $SiO_2\text{-}MnO_2$: A Bifunctional Catalyst for the One-Step Conversion of Glycerol to Acrylic Acid. *Chem. Commun.* **2014**, *50*, 9707–9710.

28. Goswami, N.; Giri, A.; Bootharaju, M. S.; Xavier, P. L.; Pradeep, T.; Pal, S. K. Copper Quantum Clusters in Protein Matrix: Potential Sensor of Pb^{2+} Ion. *Anal. Chem.* **2011**, *83*, 9676–9680.

29. Quintanar, L.; Yoon, J.; Aznar, C. P.; Palmer, A. E.; Andersson, K. K.; Britt, R. D.; Solomon, E. I. *J. Am. Chem. Soc.* **2005**, *127*, 13832–13845.

30. Williams, W. D.; Shekhar, M.; Lee, W.; Kispersky, V.; Delgass, W. N.; Ribeiro, F. H.; Kim, S. M.; Stach, E. A.; Miller, J. T.; Allard, L. F. Metallic Corner Atoms in Gold Clusters Supported on Rutile Are the Dominant Active Site during Water-Gas Shift Catalysis. *J. Am. Chem. Soc.* **2010**, *132*, 14018–14020.

31. Gianotti, E.; Shetti, V. N.; Manzoli, M.; Blaine, J. A. L.; Pearl, W. C., Jr.; Adams, R. D.; Coluccia, S.; Raja, R. Synergistic Behavior of Bimetallic Rhenium Cluster Catalysts: Spectroscopic Investigation into the Nature of the Active Site. *Chem.—Eur. J.* **2010**, *16*, 8202–8209.

32. Li, Q.; Liu, F.; Lu, C.; Lin, J.-M. Aminothiols Sensing Based on Fluorosurfactant-Mediated Triangular Gold Nanoparticle-Catalyzed Luminol Chemiluminescence. *J. Phys. Chem. C* **2011**, *115*, 10964–10970.

33. Aslan, K.; Geddes, C. D. Metal-Enhanced Chemiluminescence: Advanced Chemiluminescence Concepts for the 21st Century. *Chem. Soc. Rev.* **2009**, *38*, 2556–2564.

34. Chen, H.; Li, H.; Lin, J.-M. Determination of Ammonia in Water Based on Chemiluminescence Resonance Energy Transfer between Peroxymonocarbonate and Branched $NaYF_4$:Yb^{3+}/Er^{3+} Nanoparticle. *Anal. Chem.* **2012**, *84*, 8871–8879.

35. Chen, H.; Lin, L.; Lin, Z.; Guo, G.; Lin, J.-M. Chemiluminescence Arising from the Decomposition of Peroxymonocarbonate and Enhanced by CdTe Quantum Dots. *J. Phys. Chem. A* **2010**, *114*, 10049–10058.

36. Chance, B.; Sies, H.; Boveris, A. Hydroperoxide Metabolism in Mammalian Organs. A. *Physiol. Rev.* **1979**, *59*, 527–605.

37. Kelly, K. L.; Coronado, E.; Zhao, L. L.; Schatz, G. C. The Optical Properties of Metal Nanoparticles: The Influence of Size, Shape, and Dielectric Environment. *J. Phys. Chem. B* **2003**, *107*, 668–677.

38. Pithawalla, Y. B.; El-Shall, M. S.; Deevi, S. Laser Based Synthesis of Intermetallic Cu-Zn Nanoparticles and Filaments. *Scr. Mater.* **2003**, *48*, 671–676.

39. Zhou, Z.; Wang, Y.; Xu, D.; Zhang, Y. Fabrication of Cu_2ZnSnS_4 Screen Printed Layers for Solar Cells. *Sol. Energy Mater. Sol. Cells* **2010**, *94*, 2042–2045.

40. Bollyky, L. J. Chemiluminescence from the Reaction of Ketenes, Singlet Oxygen, and Fluorescers. *J. Am. Chem. Soc.* **1970**, *92*, 3230–3232.

41. Elbanowski, M.; Paetz, M.; Slawinski, J.; Ciesla, L. Chemiluminescence and Fluorescence of the Europium Ions-Adenine Nucleotides System and Its Possible Biological Significance. *Photochem. Photobiol.* **1988**, *47*, 463–466.

42. Lu, C.; Lin, J.-M. Carbonate-Catalyzed Chemiluminescence Decomposition of Peroxynitrite via $(CO_2)_2$* Intermediate. *Catal. Today* **2004**, *90*, 343–347.

43. Kelly, S. M.; Price, N. C. The Use of Circular Dichroism in the Investigation of Protein Structure and Function. *Curr. Protein Pept. Sci.* **2000**, *1*, 349–384.

44. Villamena, F. A.; Locigno, E. J.; Rockenbauer, A.; Hadad, C. M.; Zweier, J. L. Theoretical and Experimental Studies of the Spin Trapping of Inorganic Radicals by 5,5-Dimethyl-1-Pyrroline *N*-Oxide (DMPO). 2. Carbonate Radical Anion. *J. Phys. Chem. A* **2007**, *111*, 384–391.

45. Zheng, W.; Wang, Z.; van Tol, J.; Dalal, N. S.; Strouse, G. F. Alloy Formation at the Tetrapod Core/Arm Interface. *Nano Lett.* **2012**, *12*, 3132–3137.

46. Zheng, W.; Wang, Z.; Wright, J.; Goundie, B.; Dalal, N. S.; Meulenberg, R. W.; Strouse, G. F. Probing the Local Site Environments in Mn:CdSe Quantum Dots. *J. Phys. Chem. C* **2011**, *115*, 23305–23314.

47. Zheng, W.; Strouse, G. F. Involvement of Carriers in the Size-Dependent Magnetic Exchange for Mn:CdSe Quantum Dots. *J. Am. Chem. Soc.* **2011**, *133*, 7482–7489.

48. Richardson, D. E.; Yao, H.; Frank, K. M.; Bennett, D. A. Equilibria Kinetics and Mechanism in the Bicarbonate Activation of Hydrogen Peroxide: Oxidation of Sulfides by Peroxymonocarbonate. *J. Am. Chem. Soc.* **2000**, *122*, 1729–1739.

49. Lane, B. S.; Vogt, M.; Derose, V. J.; Burgess, K. Manganese-Catalyzed Epoxidations of Alkenes in Bicarbonate Solutions. *J. Am. Chem. Soc.* **2002**, *124*, 11946–11954.

50. Cui, H.; Zhang, Z.-F.; Shi, M.-J. Chemiluminescent Reactions Induced by Gold Nanoparticles. *J. Phys. Chem. B* **2005**, *109*, 3099–3103.

51. Stawinska, D.; Stawinski, J. Chemiluminescence of Cereal Products II. Chemiluminescence Spectra. *J. Biolumin. Chemilumin.* **1998**, *13*, 13–19.

52. DeCorpo, J. J.; Baronavski, A.; McDowell, M. V.; Saalfeld, F. E. Formation of Carbon Dioxide Dimer in Chemiluminescent Reactions. *J. Am. Chem. Soc.* **1972**, *94*, 2879–2880.

53. Jin, L.; Shang, L.; Guo, S.; Fang, Y.; Wen, D.; Wang, L.; Yin, J.; Dong, S. Biomolecule-Stabilized Au Nanoclusters as a Fluorescence Probe for Sensitive Detection of Glucose. *Biosens. Bioelectron.* **2011**, *26*, 1965–1969.

54. Lin, J.-M.; Arakawa, H.; Yamada, M. Flow Injection Chemiluminescent Determination of Trace Amounts of Hydrogen Peroxide in Snow-Water Using KIO_4-K_2CO_3 System. *Anal. Chim. Acta* **1998**, *371*, 171–176.